Understanding biases in measurements of molecular cloud kinematics using line emission

Yuxuan (宇轩) Yuan (原) [1]* Mark R. Krumholz [1,2] and Blakesley Burkhart[3,4]

[1]*Research School of Astronomy and Astrophysics, Australian National University, Canberra, ACT 2601, Australia*
[2]*ARC Centre of Excellence for Astronomy in Three Dimensions (ASTRO-3D), Canberra, ACT 2601, Australia*
[3]*Center for Computational Astrophysics, Flatiron Institute, 162 5th Avenue, New York, NY 10010, USA*
[4]*Department of Physics and Astronomy, Rutgers University, 136 Frelinghuysen Rd, Piscataway, NJ 08854, USA*

ABSTRACT

Molecular line observations using a variety of tracers are often used to investigate the kinematic structure of molecular clouds. However, measurements of cloud velocity dispersions with different lines, even in the same region, often yield inconsistent results. The reasons for this disagreement are not entirely clear, since molecular line observations are subject to a number of biases. In this paper, we untangle and investigate various factors that drive linewidth measurement biases by constructing synthetic position–position–velocity cubes for a variety of tracers from a suite of self-gravitating magnetohydrodynamic simulations of molecular clouds. We compare linewidths derived from synthetic observations of these data cubes to the true values in the simulations. We find that differences in linewidth as measured by different tracers are driven by a combination of density-dependent excitation, whereby tracers that are sensitive to higher densities sample smaller regions with smaller velocity dispersions, opacity broadening, especially for highly optically thick tracers such as CO, and finite resolution and sensitivity, which suppress the wings of emission lines. We find that, at fixed signal-to-noise ratio, three commonly used tracers, the $J = 4 \rightarrow 3$ line of CO, the $J = 1 \rightarrow 0$ line of $C^{18}O$, and the (1,1) inversion transition of NH_3, generally offer the best compromise between these competing biases, and produce estimates of the velocity dispersion that reflect the true kinematics of a molecular cloud to an accuracy of ≈ 10 per cent regardless of the cloud magnetic field strengths, evolutionary state, or orientations of the line of sight relative to the magnetic field. Tracers excited primarily in gas denser than that traced by NH_3 tend to underestimate the true velocity dispersion by ≈ 20 per cent on average, while low-density tracers that are highly optically thick tend to have biases of comparable size in the opposite direction.

Key words: MHD – radiative transfer – turbulence – ISM: clouds – ISM: kinematics and dynamics – galaxies: star formation.

1 INTRODUCTION

Molecular line emission is one of our primary tools for characterizing the dense interstellar medium. Line observations are uniquely rich in that they carry information not just on the location of gas, but on its physical properties and kinematics. In particular, the velocity information provided by lines allows one to compute the mean velocity, the velocity dispersion, and a variety of higher order statistics along each line of sight. The brightest molecular lines in the Milky Way and nearby galaxies are the first few rotational lines of CO, and it has long been known that the dispersion of the CO line is much larger than would be expected due to thermal broadening alone, indicating the presence of supersonic motions (e.g. Goldreich & Kwan 1974; Liszt et al. 1974). Subsequent exploration showed that the linewidth increases systematically with the size of the region probed (e.g. Larson 1981; Solomon et al. 1987; Goodman et al. 1998; Bolatto et al. 2008), and that the difference in velocity (measured either as the difference in first velocity moments, or via the L_2 norm or a similar norm for the difference in the full spectra) between lines

of sight increases systematically with the separation of the sightlines on the plane of the sky (e.g. Issa, MacLaren & Wolfendale 1990; Ossenkopf & Mac Low 2002; Burkhart et al. 2009). Collectively, these correlations are known as the linewidth–size relation.

While the statistics of the CO line have been explored most extensively, similar large velocity spreads are also observed in many other molecular lines, including isotopologues of CO, and a variety of tracers that, for reasons of either chemistry or excitation, are more sensitive to gas denser than that traced by CO. Examples of the latter include the rotational lines of molecules such as HCN, CS, and N_2H^+, and inversion transitions of molecules such as NH_3. These molecules often show different linewidths, and different linewidth–size relations, from CO, even when both are observed along the same line of sight (e.g. Onishi et al. 1996; Goodman et al. 1998; Walsh, Myers & Burton 2004; André et al. 2007; Kirk, Johnstone & Tafalla 2007; Muench et al. 2007; Rosolowsky et al. 2008).

There have been only limited theoretical attempts to understand the relationships between the kinematics revealed by different tracers. In some cases, authors have modelled the kinematics of particular systems observed in multiple tracers (e.g. Walker-Smith et al. 2013; Maureira et al. 2017), but there have been few more general explorations. Consequently, it is not entirely certain what

* E-mail: yuanyuxuan98@gmail.com

drives the differences between tracers. For example, Hacar et al. (2016) argue that CO linewidths are larger than those seen in rarer isotopologues because opacity broadening artificially inflates the linewidth, causing flows that are actually transsonic to appear supersonic in the CO lines. However, earlier studies showed that opacity broadening of CO is not a major correction factor for measurements of the sonic Mach number (Correia et al. 2014) from linewidths, but can be very important for measurements of the Mach number from the density spatial power spectrum (Burkhart et al. 2013b). Offner et al. (2008) argue that density-dependent excitation effects explain the differences in kinematics measured with mostly optically thin tracers such as NH_3, N_2H^+, and $C^{18}O$. The problem is fundamentally difficult because the observed line emission is a complex product of many factors including the underlying gas distribution and kinematics, subtle excitation and radiative transfer effects, and finite resolution, sensitivity and beam smearing from the telescopes. All of these effects are difficult to study because they are entangled.

Our goal in this paper is to untangle the factors that drive differences in the kinematics as measured with a range of tracers. Our approach is to rely on simulations and simulated line emission. The great advantage of using simulations is that we precisely know the true underlying kinematics, and we can conduct numerical experiments that would not be possible in reality, for example separating the effects of excitation and opacity by independently turning them on and off. To this end, in this paper, we use a series of simulations of star formation in a self-gravitating, magnetized, and turbulent medium to model line observations for five tracers: CO, $C^{18}O$, HCN, NH_3, and N_2H^+. We create synthetic position–position–velocity (PPV) cubes for each, and then analyse the statistical properties of the resulting data. We use these synthetic data to untangle what drives tracer-dependent kinematics.

The structure of this paper is as follows. In Section 2, we describe the numerical simulations and methods we use. We present our results in Section 3, where we find that higher density tracers trace smaller regions and lower linewidth due to the linewidth–size relation. We discuss general findings on which tracers perform best in Section 4, and give our conclusions in Section 5.

2 METHODS

We perform our analysis on a suite of ENZO simulations that we describe in Section 2.1 (Collins et al. 2012). These simulations are part of the Catalog for Astrophysical Turbulence Simulations (CATS) and are publicly available (Burkhart et al., submitted). In order to produce synthetic PPV cubes from these simulations, we generate a table of large velocity gradient (LVG) models with the code Derive the Energetics and SPectra of Optically Thick Interstellar Clouds (DESPOTIC; Krumholz 2014). We describe our method for producing these tables, and for using them to generate PPV cubes in Section 2.2. We then describe how we model the effects of finite telescope resolution and SNR on these PPV cubes in Section 2.3. The source code and data used in this paper are available from https://github.com/yyx319/Biases-in-measurements-of-cloud-kinematics.

2.1 Simulations

We use a suite of three simulations of self-gravitating, isothermal, and magnetized gas in a periodic domain performed with the adaptive mesh refinement (AMR) code ENZO (see Bryan et al. 2014 for a general description of the code, and Collins et al. 2012 for a description of the MHD method). The initial conditions for all three

were generated by a suite of unigrid simulations using the PPML code (Ustyugov et al. 2009) without self-gravity. These simulations are described in detail in Collins et al. (2012). The initial conditions include a uniform density field and magnetic field initialized along a preferred direction. The box is driven with a pure solenoidal pattern until a steady turbulent state is reached. At the end of the stirring phase, all three simulations have fully developed turbulence with virial parameter

$$\alpha_{\rm vir} = \frac{5v_{\rm rms}^2}{3G\rho_0 L_0^2} = 1 \tag{1}$$

and sonic Mach number $\mathcal{M}_s = v_{\rm rms}/c_s = 9$, where ρ_0 is the mean density in the simulation box, L_0 is the size of the box, c_s is the isothermal sound speed, and $v_{\rm rms}$ is the root-mean-square velocity. The three simulations have plasma β values $\beta_0 = 0.2$, 2.0, and 20.0, respectively.

Once statistical steady state is reached, gravity is turned on and the simulations are allowed to evolve with no further driving. We study snapshots from $t = 0$ to $t = 0.6t_{\rm ff}$ after gravity is turned on. During the self-gravitating phase, the root grid resolution is 512^3, and we add on top of this four levels of refinement by a factor of two. The refinement condition is such that the local Jeans length $L_{\rm J} = \sqrt{c_s^2\pi/G\rho}$ is always resolved by at least 16 zones. This gives an effective linear resolution of 8192.

Isothermal self-gravitating flows of the type used in our simulation suite can be rescaled to vary the gas density, length, and other parameters (see Section 4.2 for further discussion), but in order to calculate the observable emission we need to choose a particular set of physical values of the various simulation parameters. We therefore adopt the following fiducial scalings, which are typical of observed molecular clouds in the Milky Way:

$$t_{\rm ff} = 1.1 \text{ Myr} \tag{2}$$

$$L_0 = 4.6 \text{ pc} \tag{3}$$

$$v_{\rm rms} = 1.8 \text{ km s}^{-1}, \tag{4}$$

$$M = 5900 \text{ M}_\odot \tag{5}$$

$$B_0 = (13, 4.4, 1.3) \text{ μG}. \tag{6}$$

These choices correspond to adopting $c_s = 0.2$ km s^{-1} and a hydrogen number density $n_{\rm H} = 1000$ cm^{-3}. We return to the issue of scaling in Section 4.2.

2.2 Line emission calculation

We calculate the observable molecular line luminosity from the simulations using the code DESPOTIC (Krumholz 2014). We perform these calculations for the following lines: HCN J =1 → 0, CO J =1 → 0 and J =4 → 3, $C^{18}O$ J =1 → 0 and J =4 → 3, and N_2H^+ J =1 → 0 and NH_3 (1,1), as they span a wide range of densities at which they are effectively excited. We are particularly interested in different lines and transitions of CO and its isotopolgues, since these lines are bright and they are often used for wide-field mapping; we use the J =4 → 3 line as an example that should be representative of transitions at intermediate J in general. We do not include ^{13}CO as a separate case, because testing shows that the results for it are just intermediate between those for CO and $C^{18}O$.

DESPOTIC solves the equations of statistical equilibrium for the level populations of each species, including non-local thermodynamic equilibrium effects. It uses an escape probability formalism

to treat optical depth effects. DESPOTIC implements multiple choices for how to calculate the escape probability, and for this work we use the LVG approximation (Goldreich & Kwan 1974; de Jong, Boland & Dalgarno 1980). The details of the numerical method are provided in Krumholz (2014). We use collision rate and Einstein coefficients taken from the Leiden Atomic and Molecular Database (Schöier et al. 2005) for all calculations. The underlying collision rate data for HCN are from Dumouchel, Faure & Lique (2010), for CO and C^{18}O are from Yang et al. (2010), for N$_2$H$^+$ are from Daniel et al. (2005), and for NH$_3$ are from Danby et al. (1988) and Maret et al. (2009).

Our procedure for modelling molecular line emission follows that of Onus, Krumholz & Federrath (2018): we first set the abundances of all species per H nucleus. The values we adopt are $X_{HCN} = 1.0 \times 10^{-8}$, $X_{CO} = 1.0 \times 10^{-4}$, $X_{C^{18}O} = 1.0 \times 10^{-7}$, $X_{N_2H^+} = 1.0 \times 10^{-10}$, and $X_{pNH_3} = 1.0 \times 10^{-8}$ [where pNH$_3$ indicates para-NH$_3$, the isomer that produces the (1,1) inversion transition]; these values are taken from Krumholz (2014) and Offner et al. (2008). Secondly, we assume a constant gas temperature $T = 10$ K (Onus et al. 2018). Under these assumptions, we use DESPOTIC to compute a table of the luminosity per H$_2$ molecule in each line as a function of density and velocity gradient (which determines the optical depth in the LVG approximation), in a table of values running from 10^0 to 10^{10} cm^{-3} in 100 logarithmically spaced steps in number density and 10^{-3} to 10^3 km s^{-1} pc^{-1} in 75 logarithmically spaced steps in velocity gradient. For each cell in the simulation we take the line-of-sight (LOS) velocity gradient smoothed over 8 cells, and use that plus the density to determine the line luminosity in that cell by linearly interpolating in the table. We then generate PPV cubes for each line using the software package YT (Turk et al. 2011). Each PPV cube has a resolution of $256^2 \times 200$, with a velocity range from -4 km s^{-1} to 4 km s^{-1}. The corresponding resolution of a single PPV voxel is ≈ 0.02 pc $\times$ 0.02 pc $\times$ 0.04 km s^{-1}. We generate PPV cubes along each of the cardinal axes for each simulation at times $t/t_{ff} = 0, 0.1, 0.3,$ and 0.6.

2.3 Modelling real telescopic observations

Real observational surveys always have finite signal-to-noise ratio (SNR) and finite spatial and spectral resolution. In order to compare our synthetic observations to real observations on an equal basis, we must therefore model these effects. For this purpose, we select resolutions and sensitivities typical of Galactic surveys, since the small size of our simulated region (4.6 pc) makes comparison to extragalactic studies problematic. We consider SNRs of 5, 10, and 20, a beam size of 0.1 pc, and a velocity channel width of 0.08 km s^{-1}. This spatial and spectral resolution is comparable to that of wide-area surveys such as COMPLETE (Ridge et al. 2006) or the Green Bank Ammonia Survey (Friesen et al. 2017).

Our implementation of telescope effects is as follows: we first convolve the image in each PPV velocity channel with a Gaussian beam with a size of 0.1 pc to simulate the effect of beam smearing. Secondly, we coarsen our original PPV cube to the target spatial and spectral resolution. Thirdly, we add noise to the voxels in our PPV cube. The noise assigned for each voxel is drawn from a Gaussian distribution with a dispersion that is equal to the mean luminosity in the zero-velocity channel in the noise-free map, divided by the SNR. For the purpose of the analysis below, we mask all voxels in which the total signal, after noise is added, is below 3 times the noise level. Similarly, for velocity-integrated quantities, we mask pixels for which the intensity integrated along the line of sight is lower than $I_{noise} = \sigma_{lum} \Delta v \sqrt{n_{channel}}$, where σ_{lum} is the noise level per channel,

Δv is the channel width, and $n_{channel}$ is the number of channels in the image.

3 RESULTS

In this section, we mainly focus on the snapshots of $\beta = 0.2$, and $t = 0.1t_{ff}$ and $t = 0.6t_{ff}$, using projections in which the orientation is perpendicular to the magnetic field. We discuss the dependence of the results over the full parameter space in Appendix A, where we show that our qualitative conclusions hold regardless of the snapshots we choose to analyse. For reasons of simplicity, we therefore focus on these two example cases in the main body of the paper. For the first part of this section, we use our noise-free maps at the native resolution of the simulation; we defer discussion of the biases induced by noise and finite resolution to Section 3.4.

3.1 Qualitative results

We show an example true column density map and integrated intensity maps for our seven different tracers for the case $\beta = 0.2$, t=0.1t$_{ff}$ (i.e. just after gravity is turned on) in Fig. 1. In order to facilitate comparisons between different tracers, the dynamic range is the same in every panel. We see that different tracers pick up different parts of the flow, as expected (e.g. Burkhart et al. 2013a). Due to strong optical depth effects, CO shows a smaller dynamic range in column density than is actually present, and preferentially picks out lower density regions. Conversely, dense gas tracers such as HCN, C^{18}O J = 4→3, and N$_2$H$^+$ produce emission primarily from overdense regions, and show much larger deficits along low column density lines of sight than are actually present. C^{18}O J = 1 → 0 and NH$_3$ sit in between these extremes, reproducing the dynamic range found in the true column density map relatively well.

In order to analyse the complex statistical properties of the velocity structure, in each pixel we calculate the luminosity-weighted first moment

$$\bar{v} = \frac{\int L_v v \, dv}{L} \tag{7}$$

and second moment

$$\sigma_v = \left[\frac{\int L_v (v - \bar{v})^2 \, dv}{L} \right]^{1/2}, \tag{8}$$

where L_v is the specific luminosity at velocity v and $L = \int L_v \, dv$ is the velocity-integrated luminosity. Fig. 2 shows example second moment maps for HCN and CO J = 1→ 0, as well as their ratio, for the same snapshot as shown in Fig. 1.

We summarize the second moments that we measure for each simulation snapshot and each orientation in Table 1. In this table, we report the luminosity-weighted mean second moment for each snapshot $\int L\sigma_v \, dA / \int L \, dA$, where the integral is over all pixels in the PPV cube. For comparison, we also calculate the true mass-weighted velocity dispersion $\int \Sigma \sigma_v \, dA / \int \Sigma \, dA$, where Σ is the surface density of a pixel and σ_v is the mass-weighted mean velocity dispersion along that pixel. This gives the velocity dispersion without bias from the density dependence of emission tracers or optical depth effects. For both the true and measured second moments, we distinguish between measurements in the direction parallel to the magnetic flux, which we denote $\langle \sigma_\parallel \rangle$, and measurements in the two directions perpendicular to the magnetic flux, which we denote $\langle \sigma_\perp \rangle$; since there are two cardinal directions perpendicular to the field, we list two values of $\langle \sigma_\perp \rangle$ in Table 1.
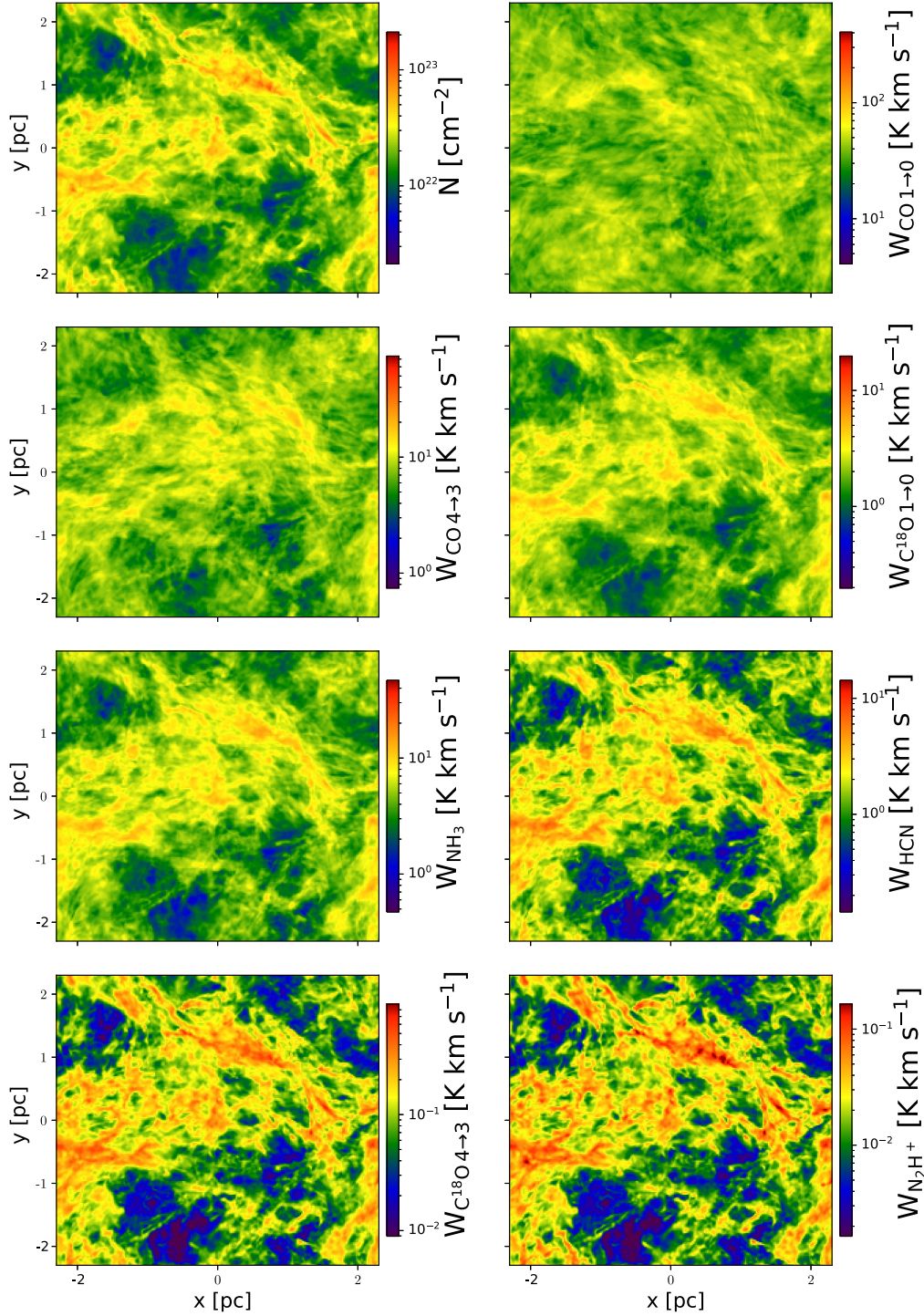
Figure 1. Velocity-integrated intensity maps for seven different line tracers as indicated in each panel for the $\beta = 0.2$ run at $t = 0.1t_{ff}$. We also show the true column density map in the top left panel. The line of sight is perpendicular to the direction of the mean magnetic field. The colour bars in each panel have a dynamic range of 100, and are all centred on the mean pixel value, enabling direct comparisons between the panels.

In both the examples shown in Fig. 2, and in the numerical values reported in Table 1, we see that our simulated maps exhibit the general trend that motivates much of this study: some tracers such as CO J = 1→0 show large, highly supersonic second moments, while others such as NH_3 or N_2H^+ show systematically smaller second moments, which approach transsonic values in some cases. Which is closest to the true, mass-weighted velocity dispersion varies depending on the observation direction and the snapshot. In the re-

mainder of this section, we investigate the physical reasons for these trends.

3.2 Density effects

One obvious difference between molecular tracers is the densities of gas to which they are sensitive. We illustrate this in Fig. 3, which shows the PDF of luminosity with respect to gas density for all the
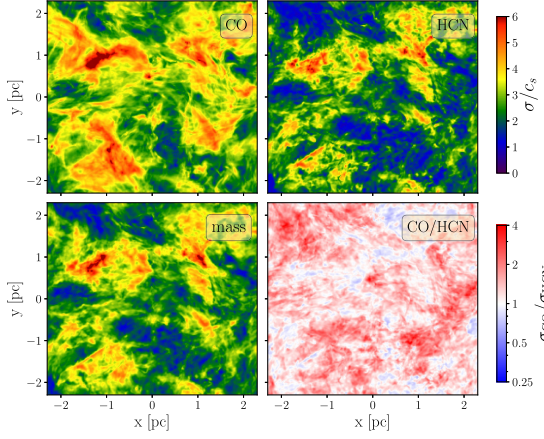
Figure 2. Luminosity-weighted second moment maps for CO J $= 1 \rightarrow 0$ (top left), HCN (top right), and for their ratio (bottom right) for the same snapshot and projection as shown in Fig. 1. The bottom left panel shows the true, mass-weighted second moment map. In all cases, the second moments we plot are normalized to the gas sound speed $c_s = 0.2$ km s^{-1}.

tracers and in the same simulation as shown in Fig. 1, at two different times, one early in the evolution ($t = 0.1 t_{\rm ff}$) and one after the collapse is well-advanced ($t = 0.6 t_{\rm ff}$). We can see that different tracers are sensitive to different ranges of density. Some, such as CO J $= 1 \rightarrow$ 0, yield a majority of their emission from gas that is less dense than the mass-weighted mean, while others, such as N$_2$H$^+$, are biased to gas that is denser than the mean; for this particular simulation, C^{18}O J $= 1 \rightarrow 0$ NH$_3$ appear to be a reasonably good tracer of the true density structure, at least near the peak of the density PDF, though this is not true of all simulations at all times.

We investigate whether differences in linewidth are caused by density-dependent emission by comparing the mean second moments with the luminosity-weighted mean density. We define the latter quantity as

$$\langle n \rangle_{\rm L} = \frac{\int n \mathcal{L} \, \mathrm{d}V}{\int \mathcal{L} \, \mathrm{d}V}, \tag{9}$$

where $\mathcal{L}$ is the luminosity per unit volume (integrated over all velocities) for a particular line and LOS as a function of position, n is the number density (measured in terms of H nuclei per unit volume), and the integral runs over the entire simulation domain. We show the relationship between $\langle \sigma_\perp \rangle$ and $\langle n \rangle_{\rm L}$ for the snapshots of $\beta = 0.2$, and $t = 0.1 t_{\rm ff}$ and $t = 0.6 t_{\rm ff}$ in Fig. 4, and report values of $\langle n \rangle_{\rm L}$ averaged over three cardinal axes for each snapshot in Table 1. We also report values of the true mass-weighted mean density, which is simply given by equation (9) with $\mathcal{L}$ set equal to the true density ρ. From the figure, we see that second moments are highly correlated with luminosity-weighted mean density. The velocity dispersion of the dense tracers can drop to trans-sonic values, despite the fact that the actual Mach number is 9, at least at early times. At later times, the luminosity-weighted mean densities tend to increase, while the velocity dispersions remain roughly constant. This is a result of the decay of turbulence and the onset of collapse. However, even deep into the collapse, we see that velocity dispersion and luminosity-weighted mean density remain highly correlated, and we therefore conclude that such correlations are a generic feature of turbulent flows, independent of whether they are self-gravitating or undergoing collapse.

The results shown above strongly suggest different lines trace different regions, and this at least partly drives the differences in

linewidth. Such behaviour is generically expected in turbulent flows, which have power spectra $P(k) \propto k^\alpha$ with $\alpha < 0$, indicating that power resides predominantly on large scales. We can verify directly that this effect is at work by characterizing the sizes of the emitting regions captured by different tracers, and checking how well these predict the velocity dispersion measured in that tracer. In order to characterize the sizes of the emitting regions, we calculate the autocorrelation function (ACF) of the luminosity density $\mathcal{L}$ for each tracer,

$$A(\mathbf{x}) = \frac{\int \mathcal{L}(\mathbf{x} + \mathbf{x}') \mathcal{L}(\mathbf{x}') \, \mathrm{d}^3 x'}{\int \mathcal{L}(\mathbf{x}') \mathcal{L}(\mathbf{x}') \, \mathrm{d}^3 x'}, \tag{10}$$

where $\mathbf{x}$ is known as the lag and the integral runs over the simulation volume. Note that we have not normalized the ACF by subtracting off the mean square of $\mathcal{L}$, because we are interested in the level of variation in the line compared to blank sky, not compared to the mean emission level of the cloud. Although our turbulence is not truly isotropic, due to the presence of a large-scale magnetic field, for convenience we will work with the angle-averaged 1D ACF, $A(x)$, which is simply the average of $A(\mathbf{x})$ over angle. In Fig. 5, we show the 1D ACF for the same snapshot as shown in Fig. 1. We see that the ACF is different for different tracers, with low-density, high-optical depth tracers like CO J $= 1 \rightarrow 0$ showing a shallow ACF, and high-density, low-optical depth tracers like N$_2$H$^+$ showing a steep ACF. For the purposes of our analysis here, we will define the characteristic autocorrelation length scale $L_{\rm AC}$ for a given tracer as the lag for which $A(L_{\rm AC}) = 0.5$. Note that this leaves $L_{\rm AC}$ undefined for CO J $= 1 \rightarrow 0$ and $4 \rightarrow 3$, since the ACF for them remains above 0.5 even for lags comparable to the size of the simulation box.

We compare the measured linewidth in each tracer with the corresponding characteristic emitting size in Fig. 6. There is clearly a near-linear correlation between $\log L_{\rm AC}$ and $\log \sigma$, where σ is the root-mean-square of the mean second moments measured along each of the three cardinal axes. We illustrate this by plotting simple linear least-squares fit to the data in Fig. 6; these fits describe the data quite well, particularly at $t = 0.1 t_{\rm ff}$. Clearly, at least part of the variation in linewidth measured with different tracers is a result of differences in density sensitivity leading to tracers picking out regions of different sizes. This, combined with the linewidth–size relation of turbulence, in turn, induces a difference in linewidth between the tracers.

3.3 Opacity effects

We next explore the effects of opacity on the linewidths measured with optically thick tracers. As pointed out by Correia et al. (2014), linewidths can be artificially enhanced by opacity broadening, whereby high optical depth suppresses emission in the line core more than in the line wings, making the line appear too broad. To begin exploring this effect, we use the cell-by-cell optical depths (which we compute using the LVG approximation) to calculate the mass-weighted mean optical depth $\langle \tau \rangle_{\rm M}$ for each of our simulation snapshots and LOS in each of our lines. We report these values averaged over three cardinal axes in Table 1. As expected, we find that CO J $= 1 \rightarrow 0$ and CO J $= 4 \rightarrow 3$ are generally very optically thick ($\langle \tau \rangle_{\rm M} \sim 1000–10\,000$), HCN and CO J $= 4 \rightarrow 3$ are moderately optically thick ($\langle \tau \rangle_{\rm M} \sim 100–1000$), and all other lines are moderately or completely optically thin.

To see how this affects the inferred velocity dispersion, in the top panel of Fig. 7 we show the distribution of second moments of our seven tracers measured in every pixel for the same sample snapshot as shown in Fig. 1. For comparison, in the middle panel, we show the same quantity, but calculated in a case where we artificially set the

Table 1. Summary of results.

Snapshot β	$t/t_{\rm ff}$	Quantity	True	CO $1 \to 0$	CO $1 \to 0$ thin	Line CO $4 \to 3$	C^{18}O $1 \to 0$	NH$_3$	HCN	C^{18}O $4 \to 3$	N$_2$H$^+$
0.2	0.1	$\log \langle n \rangle_{\rm L}$ [cm^{-3}]	3.90	3.24	–	3.49	3.76	3.75	3.96	4.10	4.21
–	–	$\langle \tau \rangle_{\rm M}$	–	1630	–	491	1.53	7.91	35.7	0.527	0.105
–	–	$\langle \sigma_{\rm II} \rangle$ [km s^{-1}]	0.59	0.71	0.58	0.64	0.61	0.59	0.52	0.47	0.45
–	–	$\langle \sigma_\perp \rangle$ [km s^{-1}]	0.58	0.73	0.57	0.64	0.60	0.58	0.52	0.47	0.45
–	–	–	0.56	0.68	0.56	0.61	0.58	0.57	0.52	0.48	0.45
0.2	0.3	$\log \langle n \rangle_{\rm L}$ [cm^{-3}]	4.39	3.25	–	3.52	3.85	3.81	4.05	4.26	4.49
–	–	$\langle \tau \rangle_{\rm M}$	–	3500	–	1060	3.27	16.7	64.8	1.16	0.155
–	–	$\langle \sigma_{\rm II} \rangle$ [km s^{-1}]	0.57	0.69	0.57	0.63	0.60	0.58	0.51	0.45	0.41
–	–	$\langle \sigma_\perp \rangle$ [km s^{-1}]	0.59	0.75	0.59	0.65	0.62	0.60	0.54	0.48	0.45
–	–	–	0.55	0.67	0.54	0.60	0.57	0.56	0.51	0.46	0.43
0.2	0.6	$\log \langle n \rangle_{\rm L}$ [cm^{-3}]	5.42	3.27	–	3.57	4.00	4.91	4.19	4.51	4.97
–	–	$\langle \tau \rangle_{\rm M}$	–	37 500	–	11 300	34.8	176	598	12.6	1.05
–	–	$\langle \sigma_{\rm II} \rangle$ [km s^{-1}]	0.54	0.69	0.54	0.62	0.58	0.57	0.49	0.44	0.40
–	–	$\langle \sigma_\perp \rangle$ [km s^{-1}])	0.61	0.77	0.60	0.68	0.65	0.63	0.56	0.50	0.45
–	–	–	0.53	0.66	0.53	0.60	0.57	0.56	0.51	0.45	0.41
2	0.1	$\log \langle n \rangle_{\rm L}$ [cm^{-3}]	3.87	3.25	–	3.48	3.73	3.73	3.93	4.07	4.18
–	–	$\langle \tau \rangle_{\rm M}$	–	1670	–	504	1.57	8.14	37.4	0.538	0.114
–	–	$\langle \sigma_{\rm II} \rangle$ [km s^{-1}]	0.57	0.65	0.57	0.62	0.59	0.58	0.53	0.49	0.47
–	–	$\langle \sigma_\perp \rangle$ [km s^{-1}]	0.51	0.57	0.51	0.55	0.53	0.52	0.49	0.45	0.43
–	–	–	0.54	0.61	0.54	0.58	0.56	0.55	0.51	0.48	0.47
2	0.3	$\log \langle n \rangle_{\rm L}$ [cm^{-3}]	4.16	3.28	–	3.54	3.85	3.82	4.05	4.25	4.45
–	–	$\langle \tau \rangle_{\rm M}$	–	3700	–	1120	3.46	17.6	68.7	1.23	0.166
–	–	$\langle \sigma_{\rm II} \rangle$ [km s^{-1}]	0.58	0.66	0.57	0.63	0.60	0.59	0.53	0.48	0.45
–	–	$\langle \sigma_\perp \rangle$ [km s^{-1}]	0.51	0.58	0.51	0.56	0.53	0.53	0.49	0.45	0.42
–	–	–	0.53	0.61	0.53	0.58	0.55	0.55	0.50	0.46	0.43
2	0.6	$\log \langle n \rangle_{\rm L}$ [cm^{-3}]	5.73	3.34	–	3.63	4.07	3.97	4.24	4.60	5.20
–	–	$\langle \tau \rangle_{\rm M}$	–	67 400	–	20 400	62.6	316	1070	22.7	1.85
–	–	$\langle \sigma_{\rm II} \rangle$ [km s^{-1}]	0.58	0.69	0.58	0.64	0.61	0.60	0.54	0.49	0.45
–	–	$\langle \sigma_\perp \rangle$ [km s^{-1}]	0.53	0.60	0.53	0.58	0.56	0.56	0.52	0.48	0.45
–	–	–	0.54	0.64	0.54	0.62	0.58	0.58	0.52	0.47	0.43
20	0.1	$\log \langle n \rangle_{\rm L}$ [cm^{-3}]	3.95	3.32	–	3.54	3.79	3.79	4.01	4.16	4.29
–	–	$\langle \tau \rangle_{\rm M}$	–	1560	–	473	1.47	7.65	35.2	0.505	0.105
–	–	$\langle \sigma_{\rm II} \rangle$ [km s^{-1}]	0.67	0.70	0.66	0.69	0.68	0.67	0.63	0.59	0.57
–	–	$\langle \sigma_\perp \rangle$ [km s^{-1}]	0.49	0.57	0.49	0.55	0.51	0.51	0.46	0.42	0.39
–	–	–	0.57	0.65	0.56	0.62	0.59	0.58	0.53	0.48	0.45
20	0.3	$\log \langle n \rangle_{\rm L}$ [cm^{-3}]	5.23	3.40	–	3.65	4.01	3.86	4.22	4.47	4.90
–	–	$\langle \tau \rangle_{\rm M}$	–	5480	–	1660	5.10	25.9	95.5	1.83	0.203
–	–	$\langle \sigma_{\rm II} \rangle$ [km s^{-1}]	0.66	0.73	0.66	0.70	0.68	0.67	0.62	0.58	0.55
–	–	$\langle \sigma_\perp \rangle$ [km s^{-1}]	0.48	0.58	0.48	0.55	0.51	0.51	0.47	0.42	0.39
–	–	–	0.58	0.67	0.58	0.65	0.61	0.60	0.55	0.50	0.46
20	0.6	$\log \langle n \rangle_{\rm L}$ [cm^{-3}]	6.35	3.53	–	4.85	4.41	4.25	4.53	5.00	5.73
–	–	$\langle \tau \rangle_{\rm M}$	–	29 600	–	8950	27.5	139	473	9.95	0.834
–	–	$\langle \sigma_{\rm II} \rangle$ [km s^{-1}]	0.65	0.75	0.65	0.68	0.67	0.64	0.58	0.56	0.54
–	–	$\langle \sigma_\perp \rangle$ [km s^{-1}]	0.56	0.68	0.56	0.64	0.60	0.60	0.55	0.49	0.45
–	–	–	0.64	0.78	0.64	0.73	0.68	0.68	0.62	0.55	0.52

optical depth of all lines to zero (or equivalently, where we take the limit of $\nabla \cdot \mathbf{v} \to \infty$ in the LVG approximation). In the bottom panel of the figure, we show the distribution of ratios of the measured to optically thin second moments; that is, the bottom panel is the distribution of the ratios of observed second moments including opacity effects (as shown in the top panel) to second moments that would be observed without opacity effects (as shown in the middle panel). From Fig. 7, we see that opacity broadening is moderately strong for CO J $= 1 \to 0$, J $= 4 \to 3$, and HCN, on average adding ~ 30 per cent to the CO-inferred velocity dispersion, and

~ 15 per cent to the HCN-inferred one. The effect is weak for all other lines.

We investigate the dependence of linewidth on opacity for the snapshots of $\beta = 0.2$, and $t = 0.1 t_{\rm ff}$ and $t = 0.6 t_{\rm ff}$ in Fig. 8. From the figure, we see that there is a weak correlation between linewidth and opacity, consistent with our earlier finding that opacity broadening is an ~ 30 per cent effect for CO J $=1 \to 0$ (Correia et al. 2014) and an ~ 15 per cent effect for HCN. Interestingly, however, there is even a correlation between linewidth and opacity for mass-weighted mean opacities $\langle \tau \rangle_{\rm M} \lesssim 1$, where optical depth effects cannot possibly be
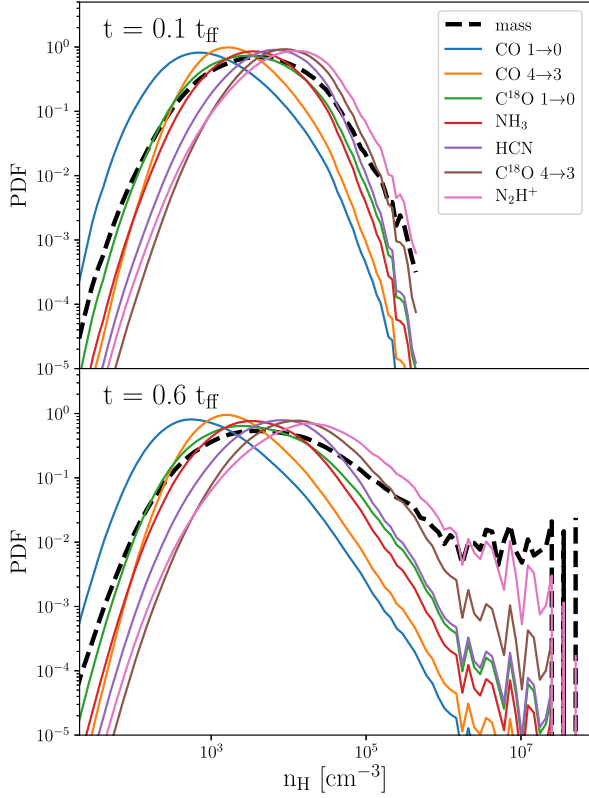
Figure 3. PDF of luminosity (coloured lines) and mass (black dashed line) as a function of log density for all the tracers for the same simulation as shown in Fig. 1 ($\beta = 0.2$) at times $t = 0.1t_{\rm ff}$ and $t = 0.6t_{\rm ff}$, corresponding to states early and late in the star formation process.
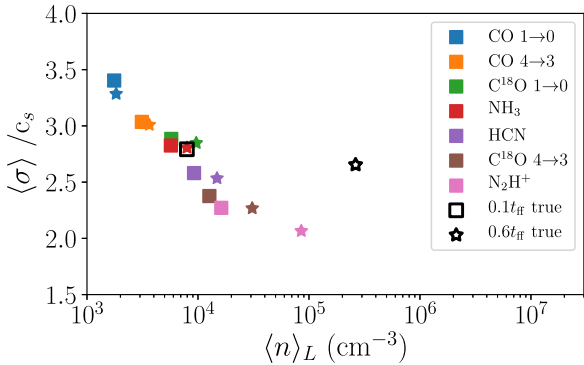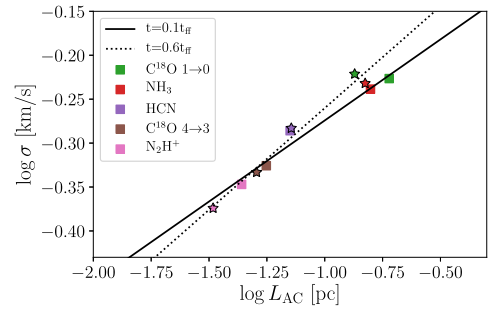

Figure 4. Luminosity-weighted second moment versus luminosity-weighted mean density in the snapshots $\beta = 0.2$, $t = 0.1t_{\rm ff}$, and $t = 0.6t_{\rm ff}$, projected along a direction perpendicular to the magnetic field; we show the data for other projections, times, and magnetic field strengths in Appendix A. Points are marker-coded by time and colour-coded by different tracers. Open symbols, labelled "true" in the legend, show the true mass-weighted mean density and velocity dispersion for each snapshot.

important – for example, Fig. 7 shows that optical depth effects are completely negligible for $C^{18}O$ J $=1 \rightarrow 0$, J $=4 \rightarrow 3$ and N_2H^+, our three most optically thin-tracers, but there is none the less a systematic trend that linewidths measured with $C^{18}O$ are larger than those measured with N_2H^+.

The reason is simple: optical depth is correlated with density sensitivity, which we have also seen affects measured linewidths. Thus, even in cases where the optical depth itself has no effect, there can
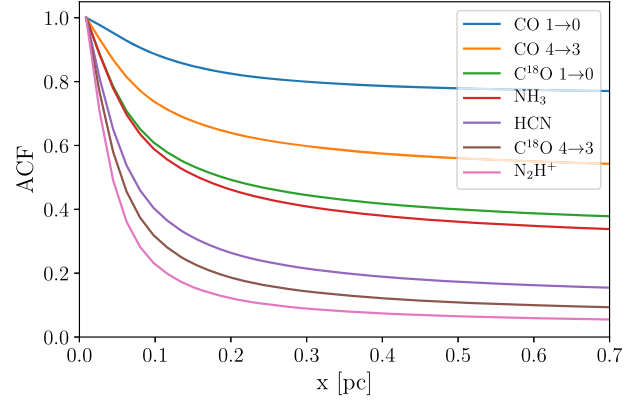

Figure 5. 1D ACF of the luminosity density for the same snapshot as shown in Fig. 1 for various tracers, as indicated in the legend.

Figure 6. Luminosity-weighted second moment averaged over cardinal directions, σ, as a function of autocorrelation size of emitting regions $L_{\rm AC}$ for the snapshots $\beta = 0.2$, $t = 0.1t_{\rm ff}$, and $t = 0.6t_{\rm ff}$. Different tracers as colour coded in the same manner as Fig. 4. The solid and dotted lines represent least-squares linear fit to the data points for the corresponding time, as indicated in the legend. Note that this plot does not include CO J = 1→ 0 and 4→ 3, because we are unable to define $L_{\rm AC}$ for them.

still be an apparent correlation between optical depth and linewidth simply because the density range to which a given molecule is sensitive affects the linewidth, and density and optical depth are correlated. The relationship is even more complex for tracers that are at least marginally optically thick, because the effective critical density for a given species depends on its optical depth – the level populations will thermalize in an optically thick region at lower density than in an optically thin one. Thus, high optical depth weights the emission to lower density regions both because it suppresses the escape of photons from higher density ones, and because it helps to thermalize the population and thus increase the luminosity in lower density ones.

In order to disentangle the various effects that optical depth has on line shape, we carry out the following experiment for CO. We first calculate the level population of CO using our normal escape probability treatment of optical depth effects, but we then calculate the resulting emission assuming the gas is optically thin. In this way, we can separate out the effects of CO optical depth on the level population from its effects on the emergent light, i.e. the effects of opacity broadening. We calculate the velocity dispersion of the PPV cubes produced in this manner using the same procedure as in Section 3.1 and show the results in Table 1. We see that the velocity dispersions computed for CO in this manner are generally very close to the values found for $C^{18}O$. This means that, at least for CO, the effect of opacity broadening is more important than the density sensitivity in setting the linewidth – i.e. when we compute the
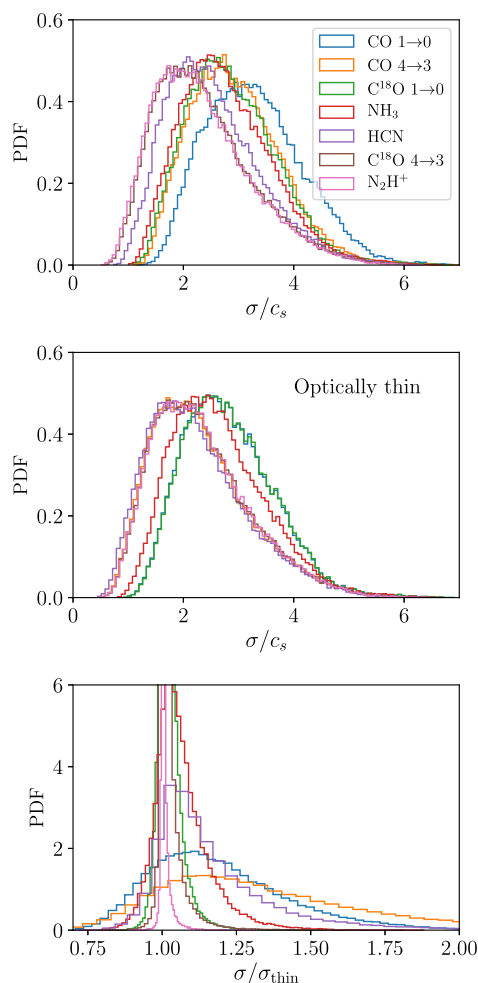
Figure 7. PDF of luminosity-weighted second moment over all pixels for the same snapshot as Fig. 1, measured along the line of sight perpendicular to the mean magnetic field. In the top panel, we show the distribution of second moments measured in each pixel using our simulated line emission, including optical depth effects in the LVG approximation. In the middle panel, we show the second moments measured from line emission where we have artificially set the optical depths of all lines in all cells to zero. The bottom panel shows the distribution of the ratios of second moments computed including and ignoring optical depth effects.

density dependence of emission including optical depth effects, but ignore the radiative transfer effects of optical depth, the linewidths we obtain are closer to the case where the optical depth is negligible for all purposes (as is the case for $C^{18}O$) than to the case where we include both optical depth effects in both the level population and the radiative transfer calculation. Conversely, for HCN, which has a more moderate optical depth and a stronger dependence on density, opacity broadening is clearly less important than density effects: while Fig. 7 indicates that opacity broadening does increase its linewidth, examination of Table 1 shows that it none the less yields a linewidth that is systematically *smaller* than the true one. For HCN, density dependence is clearly more important than opacity dependence.

Taken together, our experiments suggest that both density-dependent excitation and opacity broadening can have significant effects on inferred linewidths. For very optically thick species like CO $1 \rightarrow 0$, the opacity broadening effect is dominant. However, density-dependent excitation and the resulting variation in the characteristic sizes of emitting regions also produces a strong correlation between
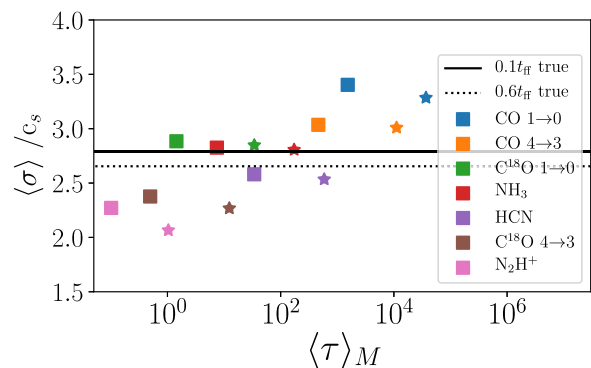
Figure 8. Luminosity-weighted mean second moment versus mass-weighted mean opacity for $\beta = 0.2$. Horizontal lines show the value of the true velocity dispersion at each time.

linewidth and the characteristic density of the emitting material. This primary correlation can also produce a spurious secondary correlation between optical depth and inferred linewidth even in species for which opacity broadening is completely negligible.

3.4 Effects of finite resolution, sensitivity and beam smearing

Finally, we investigate bias due to noise and beam smearing. In Fig. 9, we show some examples of velocity-integrated intensity maps and typical spectra before and after adding noise.[1] In the left-hand panel of Fig. 9, we see that the intensity maps are only minimally affected by noise and finite spatial resolution. However, in the right-hand panel of Fig. 9, we see that for CO $1 \rightarrow 0$, the line wings are significantly hidden by the noise, which lowers the recovered linewidth, while for HCN this effect is much smaller.

In order to illustrate the dependence of this narrowing effect on the noise level and choice of tracer, in Fig. 10 we show the ratio of the luminosity-weighted mean velocity dispersion inferred from our cubes with finite resolution and sensitivity to the true velocity dispersion. We show this ratio as a function of the SNR of the observations. For comparison, we also show results obtained from the idealized synthetic observation (infinite SNR and high resolution) as the dashed lines. We see that limited SNR can lower the inferred linewidth significantly, especially for SNR of 5 and for low-density tracers. This is because we throw out the portion of line wings contaminated by noise. In this sense, noise is the opposite of opacity effects – the latter preferentially suppress the line centre, while the former suppresses the wings. At SNR ~ 5, the linewidth we recover for CO $1 \rightarrow 0$ drops by $\sim$30 per cent compared to what we obtain in the infinite resolution limit, and even at SNR ~ 20, it is still lowered

---

[1]Careful readers may notice that the brightness temperature in the CO lines is somewhat larger than the gas kinetic temperature of 10 K. While this should not happen in reality, it can happen in our simulations due to the limitations of the LVG approximation for radiative transfer, which treats all absorption as local, and thus can miss absorption of background emission by foreground structures that are located at some distance from the emitter, but happen to overlap in velocity. This issue only affects CO, since no other tracer is optically thick enough for spatially distant foreground absorption to be significant. Moreover, by varying our method for approximating the velocity gradient, we have verified that this issue has no significant impact on our results for CO kinematics; changing our method of estimating of the velocity gradient such that the peak brightness temperature for CO changes by factors of $\sim$10 produces $\lesssim$ 10 per cent changes in the inferred velocity dispersions.
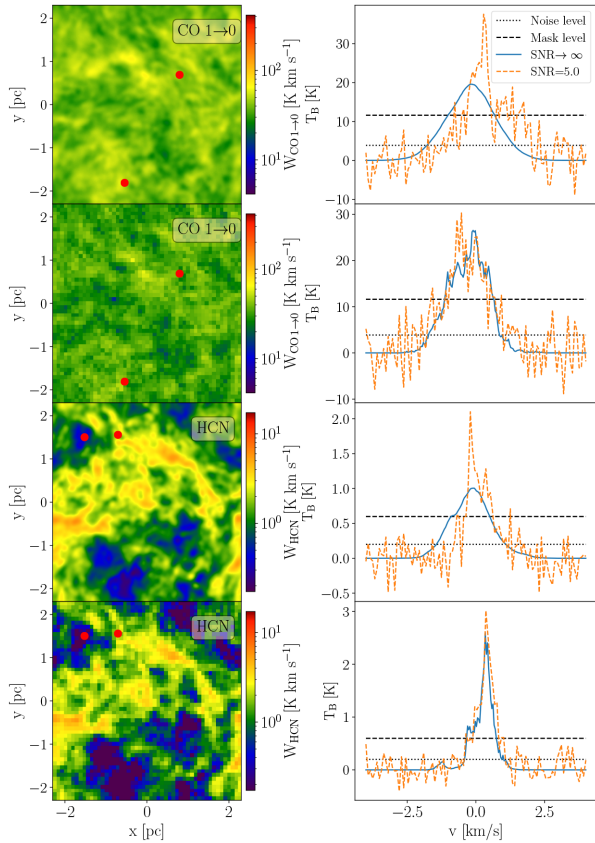
Figure 9. Velocity-integrated intensity maps (left) and two typical spectra (right) for two tracers CO 1 → 0 and HCN, for the same snapshot as Fig. 1. In the left column, the top panel for each of the two tracers shows the results for the true PPV cube, while the bottom panel shows the results after beam convolution and with a finite SNR of 5. The red circles in the map denote the positions at which we extract the two example spectra shown in the right column. In this column, we show both the true and noise-added spectra; we also show the 1σ noise level and the mask we apply at 3σ as dotted and dashed lines, respectively.
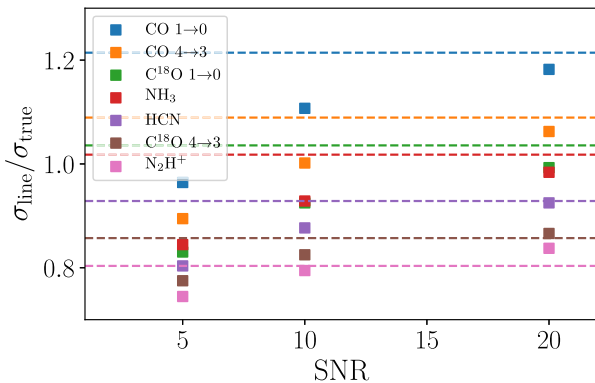
Figure 10. Ratio of the luminosity-weighted mean to true velocity dispersion, using dispersions inferred from seven emission lines as indicated in the legend, calculated from PPV cubes with finite resolution and added noise, as described in Section 2.3. We show the results as a function of the SNR. All points shown are for the same snapshot and projection as shown in Fig. 1. For comparison, results obtained from the idealized synthetic observation (infinite SNR and resolution equal to the native resolution of the underlying simulations) are shown as dashed lines.
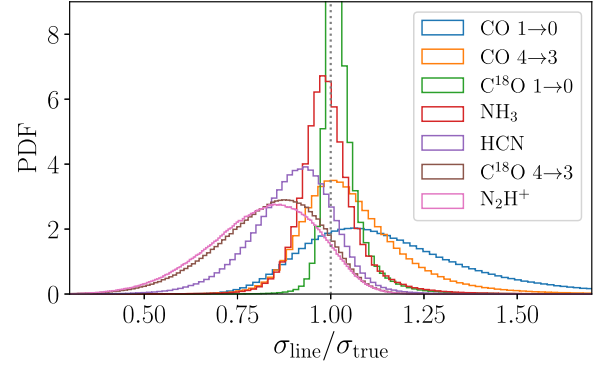
Figure 11. Distribution of ratio of the velocity dispersion measured using various emission lines, σ_{line}, to the true mass-weighted velocity dispersion, σ_{true}, for all pixels of all snapshots, i.e. combining all magnetic field strengths, times, and orientations. Different colours show different emission lines, as indicated in the legend.

by 5 per cent. For the highest density tracers such as N_2H^+, the bias induced by noise is smaller than that for the low-density tracers; for example, the N_2H^+ velocity dispersion we recover from the noisy cube is only 7 per cent smaller than for the true cube, even at an SNR of 5. Interestingly, at high SNR ~ 20, the velocity dispersion inferred from the noisy cube can even slightly exceed the value recovered from the true cube, due to the effect of beam convolution. We have verified that this is the case by also constructing PPV cubes with beam smearing but no noise – for such cubes, we find that the linewidths of the higher density tracers typically increase by a few per cent, while those of the lower density tracers are largely unaffected.

To summarize, it seems that the bias introduced by telescope is set by a competition between beam and noise effects, and the bias induced by these two components is different for different tracers. Low-density tracers are influenced significantly by noise and not affected much by beam smearing, leading to lower measured velocity dispersions, whereas high-density tracers are influenced less by noise and more by beam smearing, so that the velocity dispersion we infer for them is increased. All of these effects of resolution and sensitivity sit on top of the radiative transfer and excitation effects we have explored in the previous sections.

4 DISCUSSION

Having analysed the mechanisms that give rise to various biases, we are now in a position to draw overall conclusions about the relative reliability of various tracers, and how this depends on cloud properties. Doing so is our primary focus in this section.

4.1 Which tracers reflect the true velocity dispersion?

We begin with the most basic question: which tracers most reliably match the true (i.e. mass-weighted) velocity dispersion, and what sorts of errors and biases do these and other tracers have? To answer this question, we plot the distribution of ratio of the velocity dispersion of emission lines to the true ones for all the pixels of all snapshots in Fig. 11. We start here with the case without beam smearing or noise, and note that this histogram includes all snapshots at all times, not just the cases on which we focused as examples in Section 3. From this figure, it is clear that, overall, $C^{18}O$ is generally most accurate, with NH_3 as a close second; both have typical errors below ~ 10 per cent, and little bias, i.e. the PDF is reasonably well-centred around $\sigma_{\text{line}}/\sigma_{\text{true}} = 1$. Interestingly, we see that

CO $4 \rightarrow 3$ is also well-centred on the true value. However, its distribution is significantly broader, with errors of ~ 20 per cent. This is not surprising, since we have seen that the good average performance of CO $4 \rightarrow 3$ is due to near-cancellation between density bias and opacity bias; the latter causes pixels with high column density to show inflated linewidths, while the former causes pixels with low column density to return linewidths that are artificially low. CO $1 \rightarrow 0$ is biased high by ~ 20 per cent, and has a tail extending to > 50 per cent, while the denser tracers $C^{18}O\ 4 \rightarrow 3$ and N_2H^+ are biased low by a similar amount, and have tails extending down to a factor of 2 error.

We show in Appendix A that these general conclusions apply not just to the total distribution over all snapshots, but also to individual cases at different plasma β, orientation with respect to the magnetic field, and simulation time. It is at least somewhat surprising that which tracers are most accurate does not depend on these factors in light of Fig. 3, which shows that which lines trace the *mass* best does depend on evolutionary state – at early times when the density distribution is close to lognormal, $C^{18}O$ emission follows mass most closely, but at later times when the density distribution has developed a significant power-law tail, dense gas tracers such as N_2H^+ more accurately follow the tail of the density distribution.

The resolution to this apparent paradox can be found by noticing that, even at late times, $C^{18}O$ remains the best tracer near the peak of the PDF. We have seen that density and velocity are anticorrelated, which is why dense gas tracers tend to be biased low in their estimates of the velocity dispersion. This effect helps protect the accuracy of moderate density tracers like $C^{18}O$ and NH_3 at late times. Although there is substantial mass in the high-density power-law portion of the PDF, the bulk of the kinetic energy is still retained in the lower density material for which $C^{18}O$ and NH_3 remain accurate tracers. Thus, the material that these tracers are failing to capture makes relatively little contribution to the velocity dispersion, and thus a failure to capture it introduces little error.

Finally, let us consider how beam smearing and noise change our picture as outlined above. From the analysis in Section 3.4, we see that SNR values as low as 5 will lead to measurements of the velocity dispersion that are up to ~ 30 per cent lower than what would be recovered in the limit of infinite SNR. High-density tracers are the least affected, and become nearly insensitive to SNR once the SNR exceeds ~ 10, while low and moderate density tracers often require SNR of about 20 to approach the infinite SNR limit. Such high SNRs are generally only practical to obtain for the rotational lines of CO. This presents a challenge to observational survey design, because it is precisely such lines that suffer the most from opacity bias, and thus tend to *overestimate* the velocity dispersion when the SNR is high. Conversely, observations of tracers such as $C^{18}O$ and NH_3 that are relatively immune to density and opacity bias may often require long integration times to reach acceptable SNR. In practice, these considerations may suggest the use of CO $4 \rightarrow 3$ as the best available compromise, as it is the only line that gives a relatively precise measurement of kinematics, but is also bright enough to allow reasonable mapping speeds at high SNR.

4.2 Dependence on cloud density

As discussed in Section 2.1, in order to calculate observable line emission, we must choose a particular set of physical units for our simulation suite. It is therefore important to check to what extent our results are robust against this choice. In order to investigate this, we can rescale the simulations to arbitrary density and size scale. Since we are extracting an idealized sub-region of a molecular cloud, we
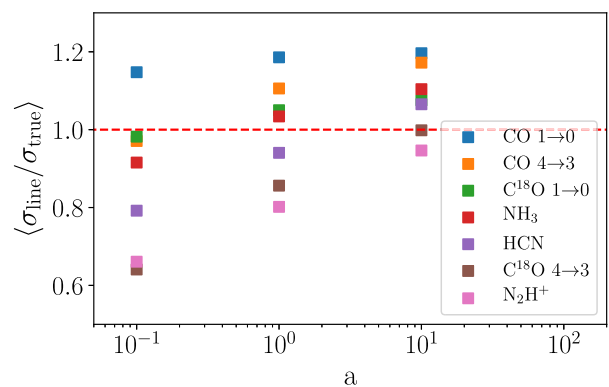
Figure 12. Ratio of the luminosity-weighted mean velocity dispersion inferred from five emission lines as indicated in the legend, averaged over all simulations snapshots and orientations and normalized to the true velocity dispersion, as a function of the density scaling factor a.

are free to regard our simulation as representing a small, dense part of the cloud, or a larger, less dense part. Quantitatively, we rescale our density field by a factor a compared to our fiducial choice, which means the average density becomes $n = 1000a\ cm^{-3}$. In the process, we have to fix the virial parameter, the Mach number, and the plasma beta, because these are all dimensionless quantities that affect the solutions to the equations of hydrodynamics. We also keep the sound speed the same, because that is set by the rate of cosmic ray heating, which is roughly constant in the Galaxy. In order to satisfy these constraints, we adopt following scalings for our rescaled simulation:

$$t_{ff} = 1.1 \times a^{-\frac{1}{2}}\ \text{Myr} \tag{11}$$

$$L_0 = 4.6 \times a^{-\frac{1}{2}}\ \text{pc} \tag{12}$$

$$v_{rms} = 1.8\ \text{km s}^{-1}, \tag{13}$$

$$M = 5900 \times a^{-\frac{1}{2}}\ M_\odot \tag{14}$$

$$B_0 = (13, 4.4, 1.3) \times a^{\frac{1}{2}}\ \mu G. \tag{15}$$

With these choices, all dimensionless numbers describing the flow are left unchanged.

We consider $a = 0.1$ and $a = 10$ in addition to our standard case $a = 1$, and generate PPV cubes and velocity dispersion measurements for all pixels in all snapshots following the same procedure described in Section 2 and Section 3.1. In Fig. 12, we show the luminosity-weighted mean velocity dispersion inferred from all our molecular species, averaged over all simulations snapshots and orientations and normalized to the true velocity dispersion, versus the density scaling factor. We see that our conclusion that $C^{18}O\ 1 \rightarrow 0$ is generally best, with NH_3 close behind, holds over a wide range of density, but that the amount of bias in these two species and in other tracers is density dependent. Lower density clouds suffer less opacity broadening and worse density bias, and thus make CO $1 \rightarrow 0$ closer to accurate and dense gas tracers further away from reality. Denser clouds have the opposite trend, suffering more opacity bias and less density bias, so that nearly any dense gas tracer works equally well, but CO is quite bad, with ~ 30 per cent errors.

4.3 Limitations of periodic boxes

In addition to worrying whether our results depend on our choice of density scale, we can also worry that they depend on

geometry. Our simulations are periodic boxes representing the central regions of molecular clouds, while real molecular clouds have dense material concentrated towards the centre, surrounded by more diffuse molecular material toward the cloud's edge. It is therefore important to consider the extent to which our use of the periodic box approximation might affect our conclusions. Kowal, Lazarian & Beresnyak (2007) have studied this question by comparing uniform-density periodic boxes such as ours to simulations in which an overall density gradient is applied on top of the periodic box, creating an effective boundary to the cloud. They find that the boundary of the molecular cloud increases the proportion of low-density gas due to the disturbance of the diffuse ambient medium. This has the effect of increasing the amount of emission per unit total cloud mass from low-density tracers such as CO $J = 1 \rightarrow 0$, but does not affect the high-density part of the density PDF, and thus has a small effect on high-density tracers, particularly $C^{18}O$ $J = 4 \rightarrow 3$, HCN, and N_2H^+. Thus, the only line for which our results are potentially affected by our use of a periodic box is CO $J = 1 \rightarrow 0$. Moreover, the direction of the bias from observation of any particular tracer depends on the extent to which that tracer departs from the "true" mass distribution. The presence of a cloud boundary will change the "true" mass-weighted density PDF and the corresponding luminosity-weighted PDF of the tracers, but the correlation between the tracers and underlying mass is the same. Thus, the direction of bias for CO is likely to be the same even in the presence of a cloud boundary. We therefore conclude that the main likely effect of adding a boundary layer to our cloud would be to change the absolute amount, but not the direction, of the bias for CO $J = 1 \rightarrow 0$. Other results would change minimally.

5 CONCLUSIONS

In this paper, we investigate the factors that drive differences in the linewidths of molecular clouds measured with various tracers. We carry out this investigation using a suite of self-gravitating MHD simulations of molecular clouds, covering a wide range of magnetic field strength and evolutionary state. For each of our sample simulations, we model the line emission using a large-velocity gradient approximation applied cell-by-cell to create synthetic PPV cubes that we use to investigate cloud kinematic structure in a variety of tracers. We specifically explore the effect of density-dependent emission and opacity broadening on observed linewidths, two mechanisms that have been discussed in the literature before, but never systematically investigated together. We also explore the effects of finite resolution and SNR. The major findings of this paper are summarized below:

(i) Molecular lines that are sensitive to denser gas tend to produce systematically lower estimates of the gas velocity dispersion. This is a direct consequence of the linewidth–size relation obeyed by turbulent molecular clouds: tracers that are excited primarily in high-density gas tend to produce most of their emission from compact regions that, as a result of the linewidth–size relation, have small velocity dispersions and thus underestimate the true velocity dispersions of large clouds. Low-density tracers, by contrast, sample larger regions and therefore return larger velocity dispersions that are closer to the true velocity dispersion.

(ii) Opacity broadening also introduces a significant bias in the linewidths measured with optical thick tracers like CO $J = 1 \rightarrow 0$. The effect here tends to be opposite to the density bias: tracers that are easily excited in low-density gas, such as CO, tend to have high optical depths near line centre. This preferentially suppresses emission from the line centre, biasing inferred velocity

dispersions too high. The relationship between optical depth and density-dependent excitation is complex, because high optical depth lowers effective critical density, while sub-thermal excitation can, depending on the molecule and line, either increase or decrease the optical depth. For CO, opacity broadening appears to be the more important effect, but which factors are dominant must be determined on a line-by-line basis.

(iii) Bias induced by noise, finite spectral resolution and beam smearing from the telescope is mainly set by a competition between beam and noise effects. Noise introduces a bias whose effect is opposite that of opacity broadening, as it contaminates the line wings significantly, which artificially reduces the inferred linewidth; low-density tracers are the most seriously affected. Beam smearing, on the other hand, increases the linewidth slightly for high-density tracers. At low SNR, the combined effects lower the linewidth of all tracers, while at high SNR, the linewidths of low-density tracers are slightly reduced, and those of high-density tracers are increased by a few per cent due to beam smearing.

(iv) The competing biases of opacity broadening and density-dependent excitation lead to a "sweet spot" where, at fixed SNR, the overall bias is minimal, for three common tracers: the $J = 4 \rightarrow 3$ transition of CO, the $J = 1 \rightarrow 0$ transition of $C^{18}O$, and the (1,1) inversion transition of NH_3. These lines generally produce the best estimates of true velocity dispersion for a typical molecular cloud, with errors below ~ 10 per cent (~ 20 per cent for CO $4 \rightarrow 3$). This statement is robust against variations of magnetic field strength, evolutionary state, and orientation relative to the direction of the overall magnetic field. By contrast, CO $J = 1 \rightarrow 0$ lines tend to produce velocity dispersions that are too large by ≈ 20 per cent, while denser gas tracers such as HCN and N_2H^+ tend to underestimate the true velocity dispersion by similar amounts. However, these biases must be weighed against those produced by finite SNR, since the $C^{18}O$ $J = 1 \rightarrow 0$ and $NH_3(1, 1)$ lines tend to be faint, and thus require longer integration times than for some other lines to reach SNR values high enough that noise does not dominate the uncertainty.

(v) The level of bias in various tracers is sensitive to the mean density of the region being observed. Over a wide range of density $C^{18}O$ remains the best estimator of the true velocity dispersion, with NH_3 close behind, but that the amount of bias in these two and in other tracers is density dependent. In extreme cases, errors in the estimated velocity dispersion can be as large as 50 per cent high or low, depending on the cloud density and the choice of tracer.

DATA AVAILABILITY

The data underlying this article will be shared on reasonable request to the corresponding author.

REFERENCES

André P., Belloche A., Motte F., Peretto N., 2007, A&A, 472, 519

Bolatto A. D., Leroy A. K., Rosolowsky E., Walter F., Blitz L., 2008, ApJ, 686, 948

Bryan G. L. et al., 2014, ApJS, 211, 19

Burkhart B., Falceta-Gonçalves D., Kowal G., Lazarian A., 2009, ApJ, 693, 250

Burkhart B., Lazarian A., Goodman A., Rosolowsky E., 2013a, ApJ, 770, 141

Burkhart B., Lazarian A., Ossenkopf V., Stutzki J., 2013b, ApJ, 771, 123

Collins D. C., Kritsuk A. G., Padoan P., Li H., Xu H., Ustyugov S. D., Norman M. L., 2012, ApJ, 750, 13

Correia C., Burkhart B., Lazarian A., Ossenkopf V., Stutzki J., Kainulainen J., Kowal G., de Medeiros J. R., 2014, ApJ, 785, L1

Danby G., Flower D. R., Valiron P., Schilke P., Walmsley C. M., 1988, MNRAS, 235, 229

Daniel F., Dubernet M. L., Meuwly M., Cernicharo J., Pagani L., 2005, MNRAS, 363, 1083

de Jong T., Boland W., Dalgarno A., 1980, A&A, 91, 68

Dumouchel F., Faure A., Lique F., 2010, MNRAS, 406, 2488

Friesen R. K. et al., 2017, ApJ, 843, 63

Goldreich P., Kwan J., 1974, ApJ, 189, 441

Goodman A. A., Barranco J. A., Wilner D. J., Heyer M. H., 1998, ApJ, 504, 223

Hacar A., Alves J., Burkert A., Goldsmith P., 2016, A&A, 591, A104

Issa M., MacLaren I., Wolfendale A. W., 1990, ApJ, 352, 132

Kirk H., Johnstone D., Tafalla M., 2007, ApJ, 668, 1042

Kowal G., Lazarian A., Beresnyak A., 2007, ApJ, 658, 423

Krumholz M. R., 2014, MNRAS, 437, 1662

Larson R. B., 1981, MNRAS, 194, 809

Liszt H. S., Wilson R. W., Penzias A. A., Jefferts K. B., Wannier P. G., Solomon P. M., 1974, ApJ, 190, 557

Maret S., Faure A., Scifoni E., Wiesenfeld L., 2009, MNRAS, 399, 425

Maureira M. J., Arce H. G., Offner S. S. R., Dunham M. M., Pineda J. E., Fernández-López M., Chen X., Mardones D., 2017, ApJ, 849, 89

Muench A. A., Lada C. J., Rathborne J. M., Alves J. F., Lombardi M., 2007, ApJ, 671, 1820

Offner S. S. R., Krumholz M. R., Klein R. I., McKee C. F., 2008, AJ, 136, 404

Onishi T., Mizuno A., Kawamura A., Ogawa H., Fukui Y., 1996, ApJ, 465, 815

Onus A., Krumholz M. R., Federrath C., 2018, MNRAS, 479, 1702

Ossenkopf V., Mac Low M. M., 2002, A&A, 390, 307

Ridge N. A. et al., 2006, AJ, 131, 2921

Rosolowsky E. W., Pineda J. E., Foster J. B., Borkin M. A., Kauffmann J., Caselli P., Myers P. C., Goodman A. A., 2008, ApJS, 175, 509

Schöier F. L., van der Tak F. F. S., van Dishoeck E. F., Black J. H., 2005, A&A, 432, 369

Solomon P. M., Rivolo A. R., Barrett J., Yahil A., 1987, ApJ, 319, 730

Turk M. J., Smith B. D., Oishi J. S., Skory S., Skillman S. W., Abel T., Norman M. L., 2011, ApJS, 192, 9

Ustyugov S. D., Popov M. V., Kritsuk A. G., Norman M. L., 2009, J. Chem. Phys., 228, 7614

Walker-Smith S. L., Richer J. S., Buckle J. V., Smith R. J., Greaves J. S., Bonnell I. A., 2013, MNRAS, 429, 3252

Walsh A. J., Myers P. C., Burton M. G., 2004, ApJ, 614, 194

Yang B., Stancil P. C., Balakrishnan N., Forrey R. C., 2010, ApJ, 718, 1062

## APPENDIX A: DEPENDENCE OF RESULTS ON DIFFERENT PARAMETERS

While we investigate the effect various biases have on the linewidth for two example snapshots and orientation perpendicular to the magnetic field in the main body of the paper, in this appendix we explore the dependence of our conclusions on the following simulation parameters: plasma β, time (i.e. evolutionary state), and orientation (i.e. whether the line of sight is perpendicular or parallel to the mean magnetic field).

We first investigate whether the correlation between density and linewidth is sensitive to these parameters. In Fig. A1, we compare the linewidth with the luminosity-weighted mean density for all the snapshots and orientations. We see that the correlation remains essentially unchanged for all combinations of parameters. The greatest sensitivity is to evolutionary state, but even this dependence is weak. To go a step further, we compare the measured linewidth averaged over cardinal axis in each tracer with the corresponding characteristic emitting size in Fig. A2 for all snapshots. We see that the near-linear correlation between $\log \sigma$ and $\log L_{AC}$ holds for all snapshots. We then show the dependence of linewidth on opacity for all snapshots and orientations in Fig. A3. Again we see that the general trend is similar to that shown in Fig. 8 for all combinations of parameters.

Having illustrated that the main results in Section 3 does not change qualitatively against different parameters. Our final step is therefore to determine whether our conclusions about which lines work best depends on the simulation parameters. Fig. A4 is the same as Fig. 11 in that it shows distributions of $\sigma_{line}/\sigma_{true}$, but now with snapshots separated in bins of plasma β (top row), simulation time (middle row), and orientation (bottom row). Surprisingly, we see that there are not any obvious variations in the distributions of $\sigma_{line}/\sigma_{true}$ with these parameters: in every case, $C^{18}O$ and NH_3 are best, with errors below ~ 10 per cent, CO is biased high by ~ 20 per cent, while the denser tracers are biased low by a similar amount.
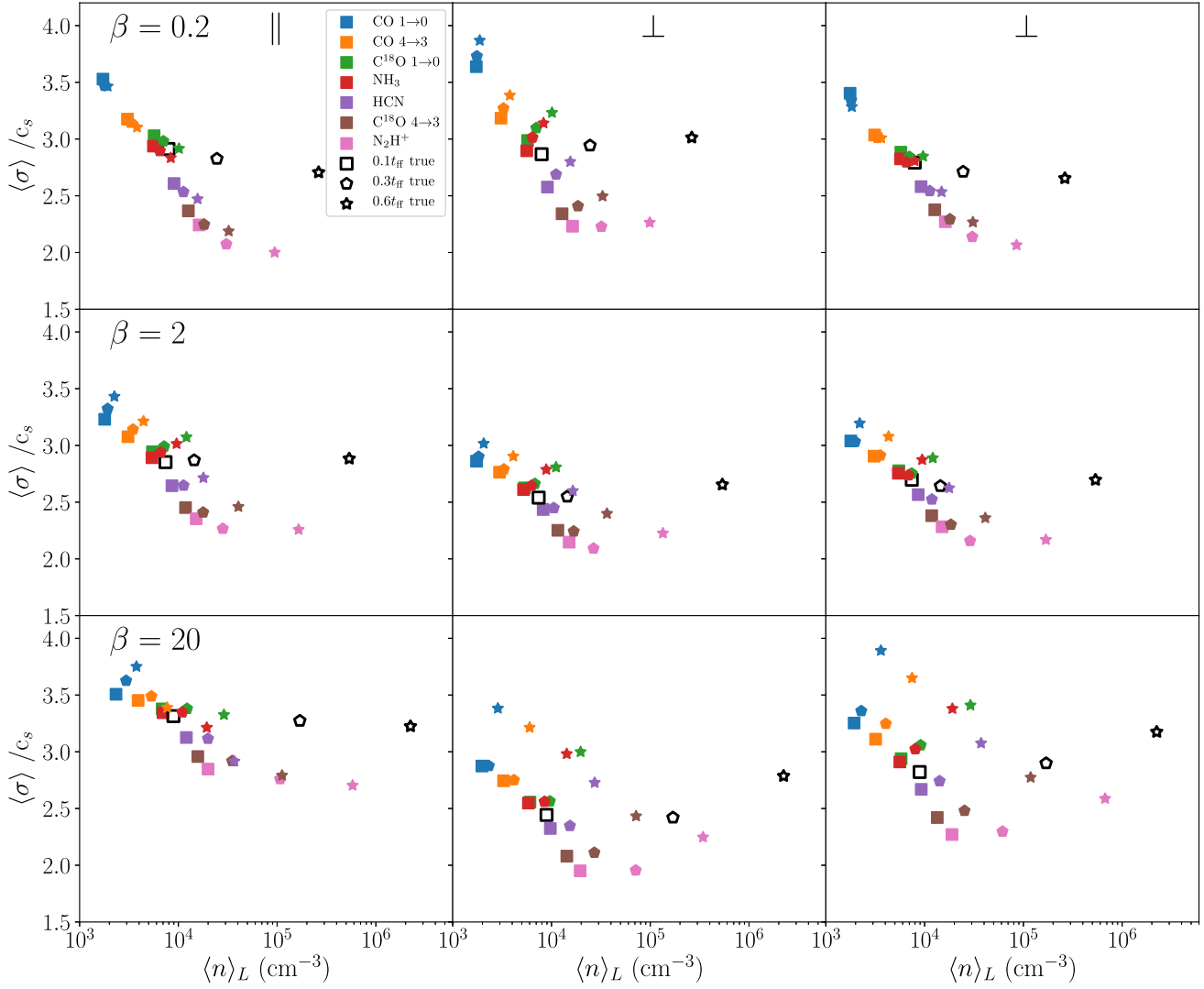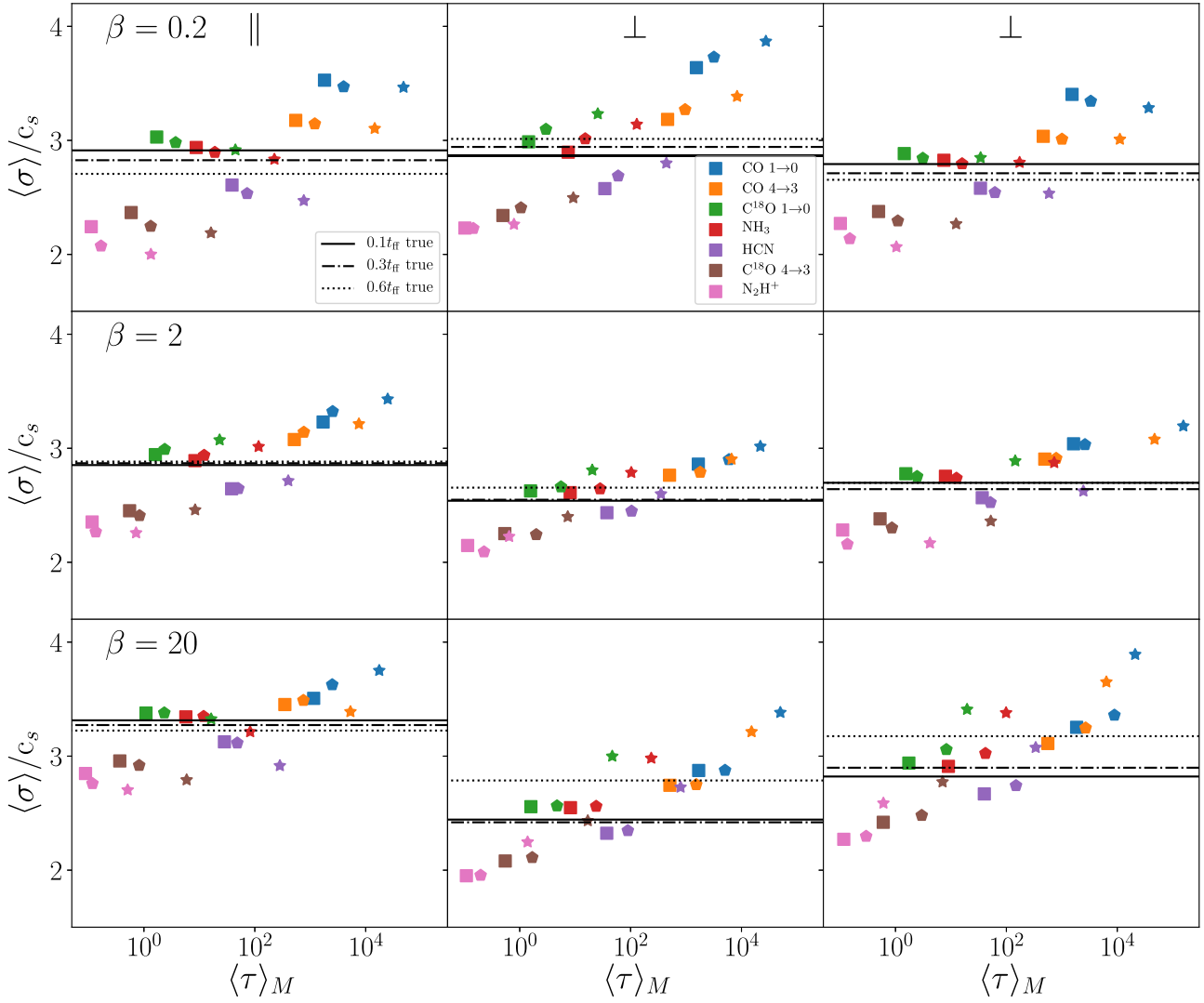
Figure A1. Luminosity-weighted second moment versus luminosity-weighted mean density for all snapshots in all simulations. We show the second moment measured along the two cardinal axes perpendicular to the mean magnetic field in the centre and right columns, and along the axis parallel to the mean magnetic field in left column. From top to bottom, we show the $\beta = 0.2$, 2, and 20 runs. Points are colour-coded by time. Open symbols, labelled "true" in the legend, show the true mass-weighted mean density and velocity dispersion for each snapshot.
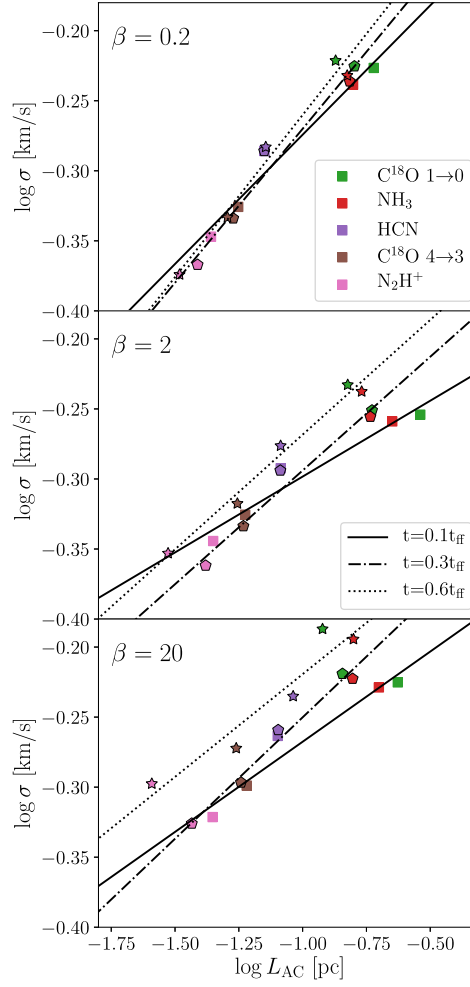
Figure A2. Luminosity-weighted second moment averaged over cardinal directions, σ, as a function of autocorrelation size of emitting regions L_{AC} for all snapshots. Lines show least-squares linear fit to the data points at the time indicated in the legend. From top to bottom, we show the $\beta_0 = 0.2$, 2, and 20 runs. Note that this plot does not include CO, because we are unable to define L_{AC} for it.

Figure A3. Luminosity-weighted mean second moment versus mass-weighted mean opacity for all snapshots in all simulations. Dotted horizontal lines show the value of the true velocity dispersion at each time.
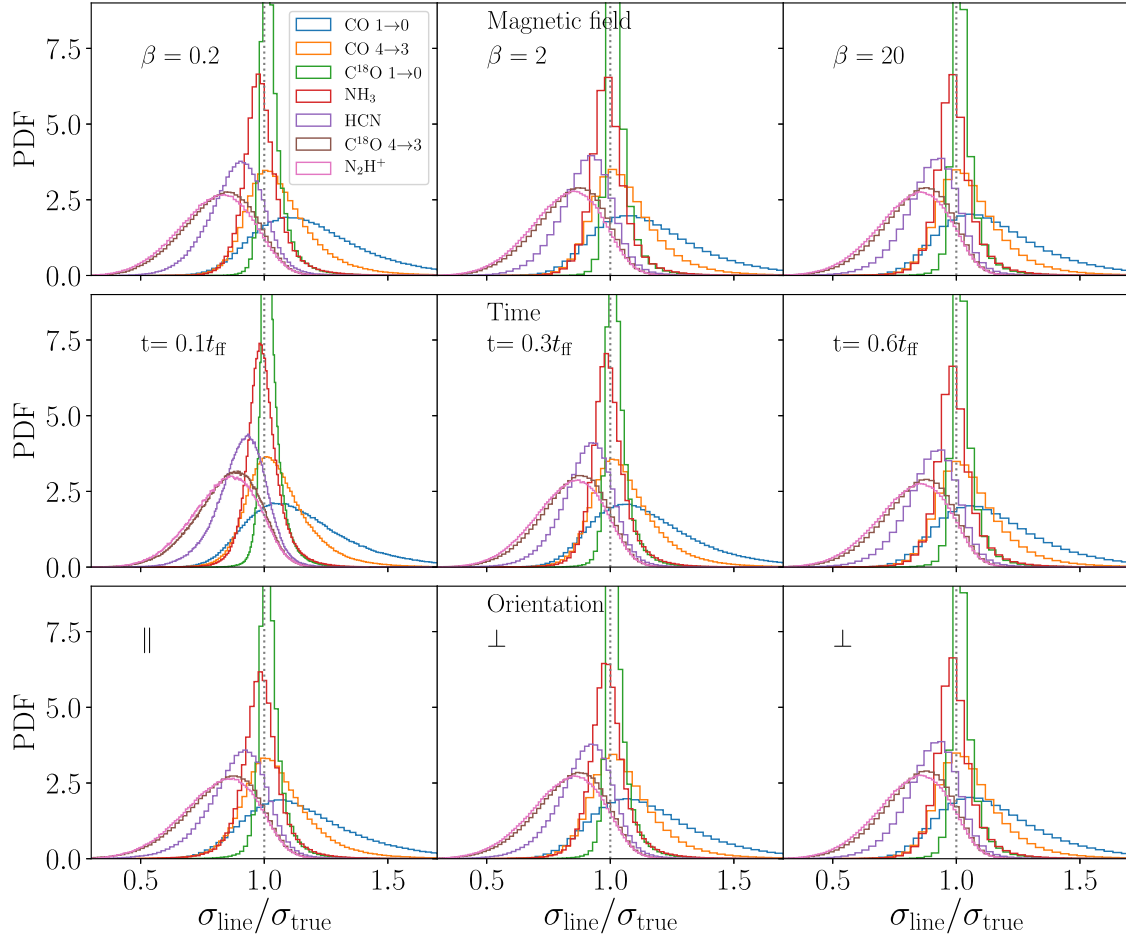
Figure A4. Same as Fig. 11, but rather than combining all snapshots of all simulations, the different rows show simulations binned by plasma β (top row), evolutionary time (middle row), and orientation relative to the magnetic flux (bottom row). In each panel, the histogram shown is for all pixels in all simulation snapshots meeting the indicated condition, e.g. the panel labelled $\beta = 0.2$ is the histogram of all pixels in all simulation snapshots and orientations for which $\beta = 0.2$.

This paper has been typeset from a TEX/LATEX file prepared by the author.